Thesis for the degree
Master of Science

Submitted to the Scientific Council of the
Weizmann Institute of Science
Rehovot, Israel

עבודת גמר (תזה) לתואר
מוסמך למדעים

מוגשת למועצה המדעית של
מכון ויצמן למדע
רחובות, ישראל

By
Elad Yaakobi

מאת
אלעד יעקבי

אפיון ושיפור מגנטומטר-קוונטי-על-חוד באמצעות קצר מובנה על חוד

SQUID-on-tip characterization and improvement using integrated resistive shunt-on-tip

Advisor:
Prof. Eli Zeldov

מנחה:
פרופ. אלי זלדוב

January 2014

שבט תשע"ד

Abstract

In this thesis we describe the work done in order to upgrade the SQUID On Tip (SOT), which is the primary tool used in our lab for magnetic microscopy. Our SOTs often exhibit hysteretic behavior which makes them unsuitable to use as magnetometers.

The main work was done in order to reduce or eliminate the hysteretic behavior by shunting the SOT with a resistive shunt deposited on the tip. According to the RCSJ (Resistively and Capacitively Shunted Josephson junction) model, reducing the normal resistance of the SQUID should increase its damping and thus reduce its hysteresis. This approach was implemented in the SOT production process.

Systematic fabrication and characterization of shunted SOTs with different parameters was carried out. We generalized the return-current parameter, which quantifies the damping in current-bias operation, to be bias mode independent. An excellent agreement with some of the RCSJ predictions was found, while other predictions were not confirmed.

The measurement circuit used to handle hysteretic SOTs was also improved by reducing the SOT parasitic resistance, so SOTs with higher negative-differential-resistance could be measured.

Using the improved measurment circuit wide variety of SOTs with different characteristics were used successfully for microscopy. The SOT optimization should be studied thoroughly though.

We also performed thorough temperature-dependence measurments, to study the temperature dependence of the critical current, the damping and the inductance. These results are also discussed here.

Contents

1 Introduction

1.1 Superconductivity

Superconductivity was first observed by Onnes in 1911 when a sudden drop in resistivity was inspected in mercury below 4.2K . In 1933 it has been discovered that the superconducting state is not merely zero resistivity but that a superconductor also expels magnetic fields.

These two phenomena are well described by the London equations,which together with the Maxwell equations, describe electromagnetism in superconductors using a phenomenological parameter Λ which is related to the density of 'superconducting electrons', n_s.

A full microscopic theory was established in 1957 by Bardeen, Cooper and Schrieffer. It describes superconductivity as a condensate of bosonic Cooper-pairs with a gapped excitation spectrum of energy gap Δ.

A phenomenological approach which concentrates on the superconducting electrons rather than the excitation spectrum was developed in 1950 by Ginzburg and Landau. It describes the superconducting phase from the point of view of second order phase transition, introducing an order parameter ψ, which is a pseudo-wavefunction for the superconducting electrons.

1.2 Josephson Effect

In 1962, Josephson predicted from microscopic theory that between two superconductors, separated by a thin insulator, called S-I-S junction, supercurrent will flow due to tunneling of cooper-pairs through the barrier. The supercurrent is given by the first (DC) Josephson relation

$$I_s = I_c \sin \delta \tag{1}$$

where δ is the phase difference between the wavefunctions across the barrier.

When applying voltage V across the junction, he predicted that the phase will evolve in time according to the second (AC) Josephson relation

$$\frac{d\delta}{dt} = 2eV/\hbar \tag{2}$$

resulting in an AC supercurrent across the junction.

Although initially deduced for S-I-S junctions, it was realized that the Josephson relations are applicable for a wide range of so called 'weak links' between two strong superconductors [1]. These junctions can be through a normal metal (S-N-S), a weaker superconductor (S-S'-S), or a narrow constriction in the material (S-c-S). For S-N-S junction with a short, one dimensional bridge, using GL theory I_c is given by $I_c = (2e\hbar\psi_\infty^2/m^*)(\mathcal{A}/L)$, where ψ_∞ is the value of the order parameter ψ deep in the interior of the superconductor, m^* is the electron effective mass in the normal metal, and $\mathcal{A}$ and L are the junction cross section area and length respectively. I_c clearly has an inverse dependence on the bridge resistance, therefore the product $I_c R_n = 2e\hbar\rho_n\psi_\infty^2/m^*$ has an invariant value which depends only on the material and the temperature. It is frequently used as a measure of how close a Josephson junction is to the theoretical limit [2].

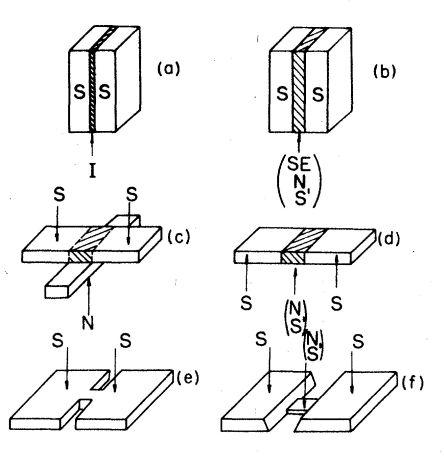

Figure 1: Different types and structures of weak-links, taken from [1]. (a) S-I-S Tunnel junction; (b) Non-tunneling sandwich; (c) Proximity effect bridge; (d) ion-implanted bridge; constriction junctions- (e) Dayem bridge; (f) Variable thickness bridge;

The full temperature dependence of I_c had been elaborated [3] for S-I-S tunnel junctions to be

$$I_c R_n = \frac{\pi\Delta}{2e}\tanh\left(\Delta/2kT\right) \tag{3}$$

For S-N-S junctions near T_c the GL theory is valid and gives the same dependence. Near T_c equation (3) can be estimated using BCS $\Delta(T)$ to be

$$I_c R_n = \frac{2.34\pi k}{e}(T_c - T) \approx (T_c - T)\cdot 635\ \mu\text{V/K} \tag{4}$$

Other theories have been used to evaluate the full temperature dependence of various weak links [4].

For constriction type links, several theories had been suggested, and it turns out that even in the vicinity of T_c, $I_c(T)$ might not have the linear dependence described above, depending on the exact geometry [1].

1.3 Superconducting QUantum Interference Device (SQUID)

The concept of the fluxoid was introduced in 1950 by F. London [5]. From the requirement that the order parameter ψ should be single-valued so that its phase ϕ has to obey $\oint \nabla\phi \cdot ds = 2\pi n$, combined with the GL equation $m^* v_s = p_s - \frac{e^* A}{c} = \hbar\nabla\phi - \frac{e^* A}{c}$ one obtains the quantization condition [2]

$$\Phi' = \frac{c}{e^*} \oint \left(m^* v_s + \frac{e^* A}{c} \right) \cdot ds = \Phi + \left(\frac{4\pi}{c} \right) \oint \lambda^2 J_s \cdot ds = n \frac{hc}{e^*} = n\Phi_0 \quad (5)$$

where A is the vector potential, v_s, J_s and p_s are the condensate velocity, current and momentum, and $\lambda = \sqrt{\frac{mc^2}{4\pi n_s e^2}}$ is London penetration depth. In the absence of current this condition simply states that the flux through a superconductor should be quantized, but in the presence of currents the *fluxoid* is the quantized quantity.

When we consider a superconducting loop with two weak links [6], the flux can be written as [2]

$$\Phi = \oint A \cdot ds = (\Phi_0/2\pi) \int_{electrodes} \nabla\phi \cdot ds + \int_{links} A \cdot ds \quad (6)$$

Because the wavefunction must be singlevalued, we can replace $\int_{electrodes} \nabla\phi \cdot ds$ by $-\sum \Delta\phi_i + 2\pi n$. Then we get the condition

$$\delta_1 - \delta_2 = 2\pi \frac{\Phi}{\Phi_0} \quad (7)$$

where $\delta \equiv \Delta\phi - (2\pi/\Phi_0) \int A \cdot ds$ is the gauge invariant phase difference that appears in equation (1), and we take the phase difference in both junction to be from electrode A to B (see Fig. 2).

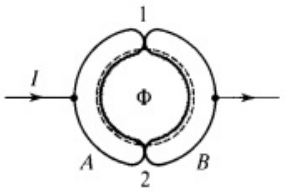

Figure 2: A schematic drawing of a SQUID. A current is driven from electrode A to B, which compose a superconducting loop with two weak-links 1,2.

This condition implies that unless Φ is an integral multiplication of Φ_0, both junctions cannot simultaneously have $\delta = \pi/2$, so the maximal supercurrent from A to B depends periodically on the magnetic flux. In the special case when both junction are identical, i.e. $I_{c1} = I_{c2} = I_0$, then one can obtain for the maximal supercurrent

$$I_c = 2I_0 |\cos(\pi\Phi/\Phi_0)| \quad (8)$$

where I_0 will denote the junction intrinsic critical current.

This dependence is the basis of SQUID magnetometry, which allows us to measure flux fractions of Φ_0.

Since it is not practical to directly measure I_c, the common operation [7] is to bias the SQUID with a current slightly above I_m and measure the modulation in voltage on the SQUID, so at a certain working current the SQUID is a flux to voltage transducer.

The actual flux is not necessarily equal to the applied flux, because non-negligible screening can be caused by circulating current in the SQUID loop. Condition (7) must still hold, but now the total flux is modified by $\Phi_{screening} = L_g J$, where L_g is the loop inductance. Kinetic inductance also causes a phase difference between the two SQUID arms, which can be taken into account as 'effective flux' that can be written as $L_k J$. So we can write $\Phi_t = \Phi_{app} + (L_k + L_g)J = \Phi_{app} + LJ$ [9]. The circulating current J is given by

$$J = (I_0/2)(\sin\delta_2 - \sin\delta_1) \tag{9}$$

This screening causes the critical current to have lower modulation, because the circulating current will 'push' the total magnetic flux toward integral multiplication of Φ_0. The modulation depth will decrease down to 50% for $\beta_L \equiv \frac{2LI_0}{\Phi_0} = 1$ and much more drastically for $\beta_L \gg 1$ (see Fig. 3).

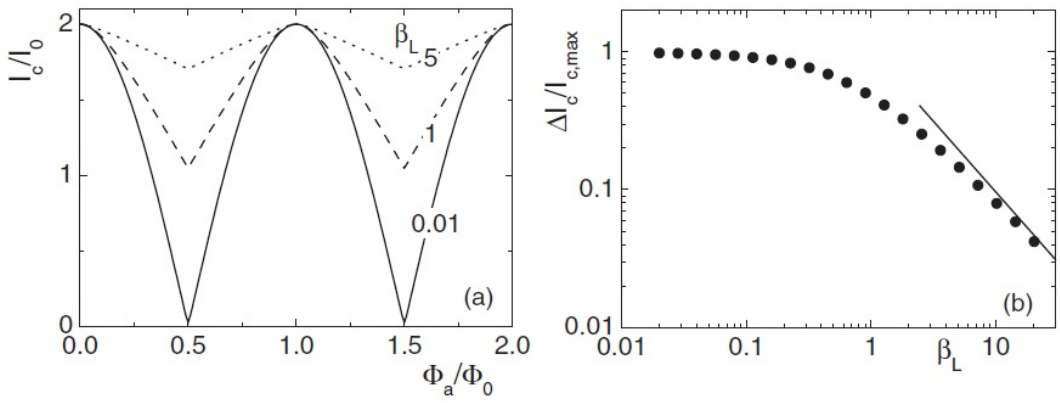

Figure 3: (a) I_c modulation for various values of β_L and (b) modulation depth vs. β_L. Taken from [7].

For large values of β_L there might be two possible Φ_t for the same applied Φ_{app}, which can cause magnetic hysteresis [2]. We will not deal with that issue in this work.

1.4 The SQUID On Tip (SOT)

While larger SQUIDs have better field sensitivity, for purposes of microscopy a good spatial resolution is required, so the SQUID dimensions have to be small enough to resolve the details in the sample. In order to achieve better resolution it is essential that a scanning device can be brought into close proximity with the sample. Moreover, since the field of a magnetic dipole decreases as r^{-3}, approaching closer to the sample is critical for magnetic microscopy [8]. Using lithographical methods, planar SQUIDs in the submicron regime have been successfully fabricated, however their planar geometry limits the distance they can approach to the sample [10].

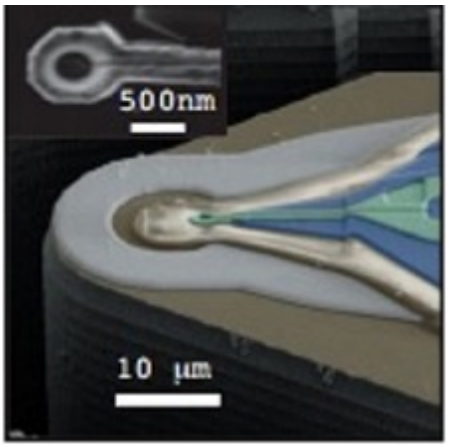

(a) The FIB design of a planar SQUID, taken from [10], the inset shows an AFM image of the pickup loop.

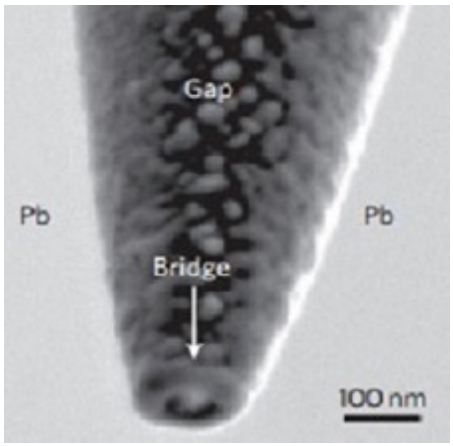

(b) A SEM image of a Pb SOT. The two solid Pb banks are the electrodes, the bridge is the weak link.

Figure 4: Nanoscale SQUIDs.

In our lab, a nano SQUID on a tip (SOT) has been developed (see Fig. 4)[11, 12, 13, 14]. SQUID loop and contacts are deposited on a quartz pipette with an apex diameter of about hundred nanometers, in a process described in section 3.1.This geometry is ideal for scanning microscopy and this powerful tool is used in our lab to study magnetic properties and dynamics of vortex matter, topological insulators and efforts are made to measure the magnetic field due to a single spin [8].

1.5 RCSJ Model

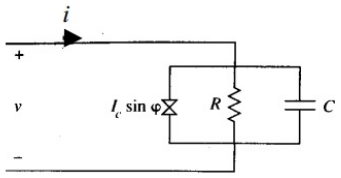

Figure 5: The RCSJ model

Under finite voltage a more complete description of the junction is required. The Resistively and Capacitively Shunted Josephson Junction (RCSJ) model includes quasiparticle ('normal') current as well as displacement current due to voltage changes on the junction, these two are modeled by a resistor and a capacitor in parallel with the ideal Josephson element. The total current through the junction is the sum of the supercurrent given by eq. (1), the normal current $I_{qp} = V/R$ and the displacement current $I_d = C\dot{V}$ (see Fig. 5). The voltage can be written in terms of the phase difference using the second Josephson relation (eq. (2)), and we can write

$$I = I_c \sin\delta + \frac{\Phi_0}{2\pi} C\ddot{\delta} + \frac{\Phi_0}{2\pi} R^{-1}\dot{\delta} \tag{10}$$

or in a dimensionless form

$$i \equiv \frac{I}{I_c} = \sin\delta + \beta_c \frac{\ddot{\delta}}{\omega_c^2} + \frac{\dot{\delta}}{\omega_c} \tag{11}$$

where $\omega_c \equiv 2\pi I_0 R/\Phi_0$ is the Josephson frequency at the characteristic voltage $V_c = I_c R$ and $\beta_c \equiv \frac{2\pi}{\Phi_0} I_0 R^2 C = \omega_c RC$ is the ratio between the resistance R and the capacitor impedance at typical Josephson frequency $\frac{1}{\omega_c C}$, which indicates whether the junction is shunted through the capacitance or also by the resistor [15, 16].

The RCSJ 'equation of motion', with the coordinate ϕ is the phase difference, is equivalent to that of a driven, damped pendulum, with equation of motion $\tau = mg \cdot \sin\phi + I\ddot{\phi} + \gamma\dot{\phi}$, where τ is an applied torque, I is the moment of inertia and γ is the friction coefficient, and ϕ is the angular coordinate.

This analogy gives instructive intuition. For applied torque smaller then mg the system has a static equilibrium at some angle ϕ_0, this is equivalent to DC supercurrent with constant phase δ_0. At torque larger than mg the pendulum will rotate, and friction will take place.

In the overdamped case ($\beta_c \ll 1$), without sufficient torque to overcome gravity the pendulum cannot rotate, and it will lose all its kinetic energy and stabilize in a static equilibrium.

On the opposite limit, the underdamped case ($\beta_c \gg 1$), energy is conserved and rotational motion can exist even without applied torque, given enough energy.

Thus for any current driven, even below I_c where a DC solution is valid, there exists an AC configuration. The minimal current for which there exists an AC configuration depends on the exact value of β_c.

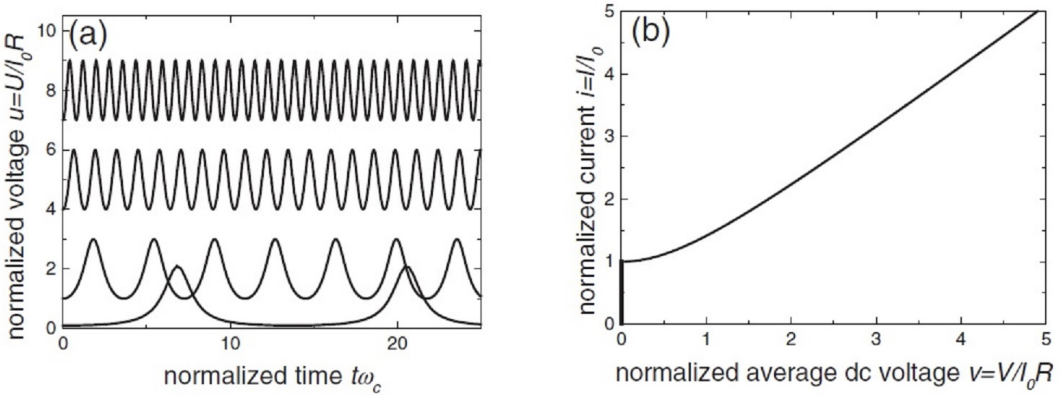

Figure 6: Characteristics for a strongly overdamped junction calculated within RSJ: (a) Normalized voltage vs. time for normalized bias currents of (bottom to top) $i = 1.1, 2, 5$ and 8; It can be seen that whereas at high currents the voltage is nearly harmonic, thus the time integrated supercurrent vanishes, resulting in an ohmic I-V, at low currents the voltage is an anharmonic pulse train, thus the supercurrent contributes to the total current. (b) Normalized I-V.Taken from [7].

When we measure the voltage across the junction we measure the time integrated potential difference $\overline{V} = \langle V \rangle$, since the typical Josephson frequency is of order of GHz, well above the bandwidth of typical voltmeters. In the overdamped limit the RSJ equation can be solved analytically to give

$$v \equiv \frac{\overline{V}}{V_c} = \sqrt{i^2 - 1} \tag{12}$$

for $I > I_c$, see Fig. 6.

It is important to notice that while the dependence of β_c on I_c is linear, it is quadratic in R, so lowering the resistance of the junction is a more efficient way to increase the damping than lowering the critical current.

For underdamped junctions, however, for currents below I_c there is in addition to the zero voltage static solution an AC solution with nonzero voltage so the I-V curve is multivalued, and the differential resistance above I_c is negative. When driving current and increasing it from zero the voltage will stay at zero until we reach I_c, then it will jump to the voltage corresponds to the AC solution just above I_c, this leads to discontinuous response near I_c, see Fig. 7.

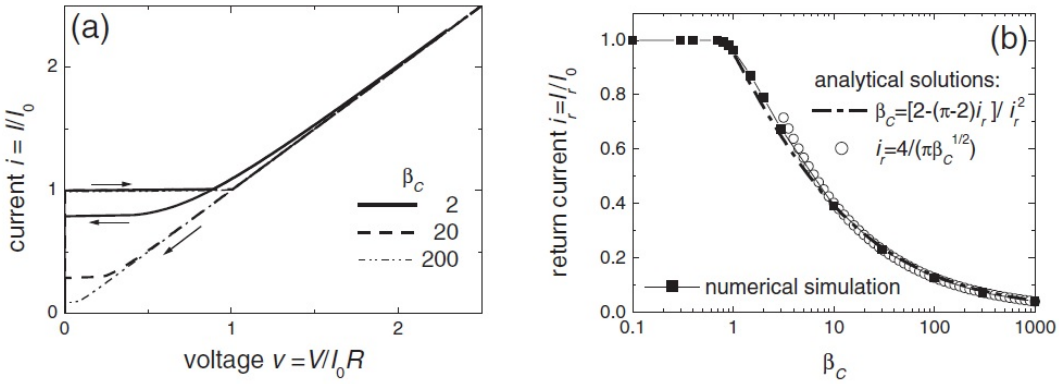

Figure 7: Hysteresis behavior at current bias: (a) Normalized I-V for various values of β_c (arrows indicate direction of bias current sweep). As the current reaches I_c ($i = 1$) the voltage jumps from zero to around I_cR, but as the current sweeps back down voltage goes back to zero only at I_r, the value of which depends on β_c; (b) normalized return current $i_r = I_r/I_c$ vs. β_c. Taken from [7].

When lowering the current back down below I_c, the voltage will continue to oscillate until the current reaches I_r, below which only zero-voltage solution is possible, then it will jump back to zero voltage. For light damping the value of $i_r \equiv I_r/I_c$ can be estimated treating the damping force as a perturbation, giving the following

$$i_r = 4/\left(\pi\beta_c^{1/2}\right) \tag{13}$$

For most practical purposes this hysteretic behavior is a problem, so junction with $\beta_c \leq 1$, at which $I_r \approx I_c$, are required. Most weak links have by nature very low capacitance so they fulfill this condition [1]. However the SOT weak links have non-negligible capacitance so they might be hysteretic.

The most efficient way of lowering β_c is by lowering R, a common way of doing this is shunting the junction externally[2, 7]. In this work we implement this concept in our SOT. We note, however, that by using an external shunt, the I_cR becomes lower then the intrinsic I_cR_N.

Applying RCSJ model to a SQUID (Fig. 8) and normalizing time to $\tau \equiv \omega_c^{-1}$,

we can write the following set, in dimensionless form,

$$\frac{i}{2}+j = (1-\alpha_I)\sin\delta_1+(1-\alpha_R)\dot{\delta_1}+(1-\alpha_C)\ddot{\delta_1} \quad (14)$$

$$\frac{i}{2}-j = (1+\alpha_I)\sin\delta_2+(1+\alpha_R)\dot{\delta_2}+(1+\alpha_C)\ddot{\delta_2} \quad (15)$$

$$\delta_2-\delta_1 = 2\pi(\phi_{app}+\frac{1}{2}\beta_L j) \quad (16)$$

where J is the circulating current, the currents are normalized to the average critical current $I_0 \equiv (I_{0,1}+I_{0,2})/2$, $\phi \equiv \Phi/\Phi_0$, $R=\frac{2R_1R_2}{R_1+R_2}$, $C=\frac{C_1+C_2}{2}$, and $\alpha_{I,R,C}$ parameterize asymmetries in I_0, R and C respectively.

A basic understanding can be obtained using the simplifying assumption that the junctions are identical and the inductance is negligible ($\beta_L \ll 1$). Equations (14)-(16) then reduce to

$$i = 2\left[\cos(\pi\phi_{app})\cdot\sin\gamma+\dot{\gamma}+\beta_c\ddot{\gamma}\right] \quad (17)$$

with $\gamma \equiv \delta_1+\pi\phi_{app}$. This equation is identical to equation (11) of a single junction with resistance $R/2$, capacitance $2C$ and flux dependent critical current $2I_0\cos(\pi\phi_{app})$. Thus for a SQUID with $\beta_c \leq 1$, biased with current above the maximal critical current $2I_0$ we can approximate the signal by

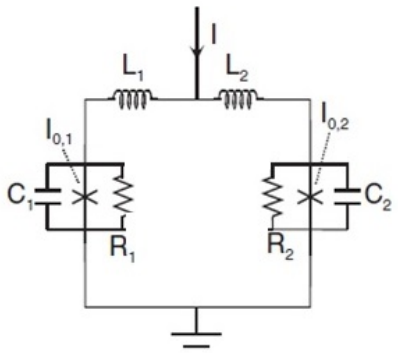

Figure 8: The RCSJ model for a SQUID.

$$V = \frac{R}{2}\left\{I^2-\left[2I_0\cos(\pi\phi_{app})\right]^2\right\}^{1/2} \quad (18)$$

The biggest flux response is clearly when the biasing is exactly at $2I_0$, the voltage then swings between 0 at $\phi_{app}=0$ and $V_0=I_0R$ at $\phi_{app}=1/2$ [7]. Note that when using an external shunt V_0 is reduced from I_cR_N which is typically of order mV.

Because practical SQUIDs are usually overdamped, their response was mainly studied in this regime ([17, 18], and [7] chapter 2), where the main effect of inductance is lowering the modulation.

1.6 Loadline Techniques, Response, SNR

When dealing with underdamped SQUIDs, in order to overcome the problem of hysteresis we use a different operation mode instead of the current biasing described above. We bias our circuit with a voltage source with a large series resistor, which is practically a current source, we denote $I_b = V_b/R_b$. An external R_s is connected in parallel to the SOT, which is connected with a parasitic resistance denoted by R_{par}, (see Fig. 9)[12, 13, 14, 8]. We then measure the current through the SOT branch using an SSAA (SQUID Series Array Amplifier) [19, 20], with a feedback box (see 3.3).

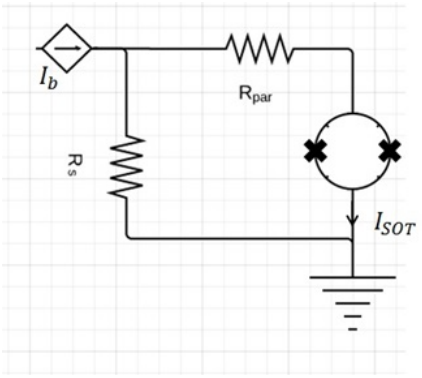

Figure 9: The operation circuit. The current through the SQUID is measured as a function of the voltage across it. The loadline is determined by the shunt and parasitic resistances.

The external circuit is coupled to the SOT using a few centimeters of wire, which at typical Josephson frequencies has a high impedance of order 100 Ω, so the Josephson oscillations take place only within the SQUID itself, and it can be treated as a DC blackbox whose I-V characteristic is governed by its intrinsic properties.

An elementary calculation gives us

$$I_{SOT} = \frac{I_b R_s}{R_p + R_s} - \frac{V_{SOT}}{R_p + R_s} \tag{19}$$

This can be graphically understood as finding the intersection of the SOT I-V curve with a 'load line' whose slope is determined by the shunt and parasitic resistances. Current biasing is equivalent to a horizontal load line, voltage biasing is a vertical load line, and our load line is in between as illustrated in Fig. 10.

It is clear that current biasing an I-V with a negative differential resistance will result in a multivalued solution. If, on the other hand, the actual load line slope is steeper than the I-V, i.e. $R_s + R_p < |r_d|$, when r_d denote the SOT differential resistance, the solution is single-valued and no hysteresis will occur.

Using this method we measure the modulation in I_{SOT} at a given I_b thus a single load line. Using simple geometrical arguments (see Fig. 11) it is easy to see that, assuming parallel I-Vs for different fluxes, the modulation measured is given

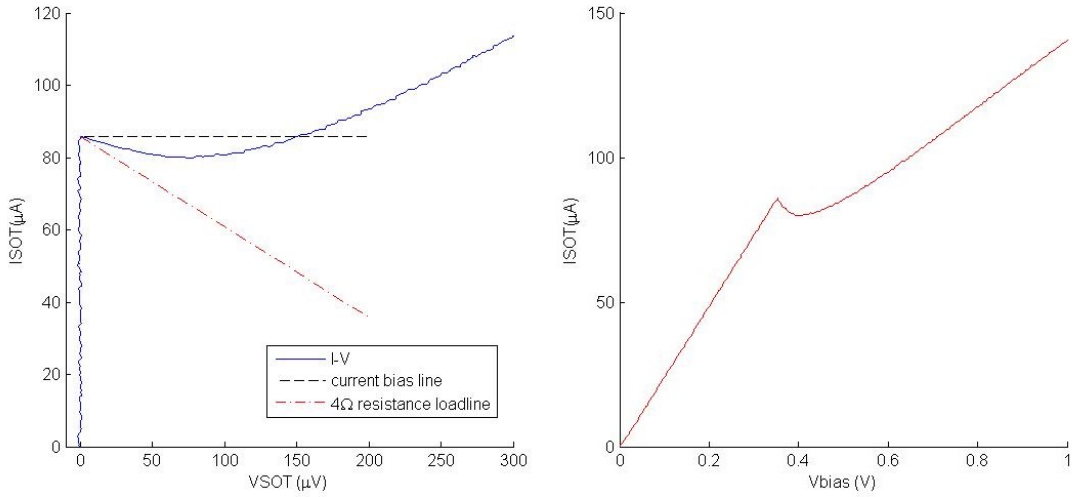

Figure 10: Left: The SOT I-V curve, the current bias loadline (dashed) and the actual loadline used to measure this SOT. While the current bias line is multivalued in the region between I_c and I_r, it is clear that at any voltage (vertical offset) the actual loadline will result in a single-valued solution. The SOT I-V data was obtained from the measured data plotted on the right, as explained later in section (3.4)

by

$$\Delta I = \Delta I_c \frac{1}{1 + r_s + r_p} = \Gamma \Delta I_c \tag{20}$$

where $r_{p,s} \equiv \frac{R_{p,s}}{r_d}$. So to maximize the response we shall make both $R_{s,p} \ll r_d$.

Noise sources in SQUIDs and optimization of the SQUID have been thoroughly studied [17, 18, 7], and further work on the SOT must be concentrated on this aspect. However, this was not in the scope of this work. On the other hand, when optimizing the operating circuit response, we must take into account the thermal noise induced by the resistors, which is believed to be the major source in our devices. Taking into account R_s, R_p and the SOT normal resistance R_N(which from now on denotes the SOT normal resistance, regardless of whether it was shunted), one gets

$$i_n = \sqrt{\frac{4k_B T \Delta f}{R_s + R_p + R_N}} \tag{21}$$

To reduce this noise one should make the resistance as large as possible, this of course is in contradiction with equation (20). Looking at the expression for the

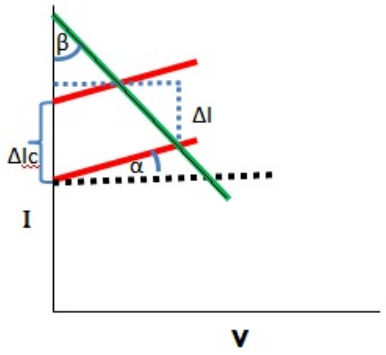

Figure 11: An illustration of the loadline dependence of the modulation. Two parallel I-Vs with ΔI_c measured by a single loadline will cause current modulation of ΔI.

SNR dependence

$$SNR \propto \frac{\sqrt{R_N + R_s + R_p}}{1 + r_s + r_p} \tag{22}$$

it is clear that while for a given r_d and R_N, R_p and R_s should be carefully optimized, r_d and R_N should be maximized. Thus we would like to tune R_N such that $\beta_c \approx 1$ for which r_d is maximal.

From RCSJ it follows that, fixing $\beta_c = 1$, we can lower R_N by a factor x and increase I_c by a factor x^2, so it seems we should try first increasing I_c, gaining a factor x^2 in response, and absorb the slight increase of the noise. Attention should be paid, however, to the fact that β_L also scales linearly with I_c, and modulation depth will also be affected.

2 Goals

The main goals of this work is to resistively shunt our SOTs, investigate the effects of different shunt parameters and optimize them.

The first challenge is to make the shunt and be able to control the shunt parameters such as location on the tip and resistance. The shunt has to be located very close to the tip apex, as described below, so an accurate process of *in situ* deposition on the tip has to be developed and implemented.

The first inquiry to be made is to look for agreement with RCSJ, i.e. the dependence of damping on I_c, R and C, both for zero field case, where screening can be neglected, and for applied magnetic field, where the validity of equation (17) can be tested.

Another open question for this work is the effect of shunt location on the damping, since parasitic inductance of the coupling between the shunt and the junction will not be negligible at high frequency. The possible effects range between correction of the RCSJ capacitance to larger 'effective capacitance' [21], to 'current limited damping', where the shunt can support only fraction of the current, and RCSJ is not valid any more [22]. On the other hand a too close shunt might suppress the Josephson junction critical current due to proximity effect.

Optimization means firstly that we gain enough control in the fabrication process and knowledge so that we can make SOTs with desirable damping. Secondly, we should find the optimal damping. In current bias operation, the optimal response is obtained for $\beta_c \approx 1$ [7]. We should study the behavior under loadline operation.

Recently we started to study the SOT behavior at different temperatures, where we study

- The critical current temperature dependence and agreement with Eq. (4).
- The damping temperature dependence, as a consequence of the change in I_c.
- The inductance temperature dependence, and its effect on the damping.

As for the inductance, since $\beta_L \propto I_c$ we expect its effect to be smaller at higher temperature. But, since the estimated inductance in our SOTs, taken from modulation depth (as shown in section 3.5 and 4.6), is of order 10 pH, two orders of magnitude larger than the geometrical estimated inductance [8], we suspect

that the major contribution is from the kinetic inductance, which is inversely proportional to the charge carrier density n_s, we thus expect the inductance to increase with temperature. This also has been subjected to study.

3 Methods

3.1 Tip Fabrication

We use quartz tubes with inner diameter 0.5 mm and outer diameter 1 mm. We pull them using a commercial Sutter Instruments P2000 micropipette puller. The pulling process consists of several steps that can have different parameters resulting in different pippete geometry. The tube is inserted into two bases on both edges, which have springs that apply force to pull them apart. The tube is then heated in the center using a CO_2 laser beam, while being pulled from the edges. After the tube is pulled softly a 'hard pull' is initiated. A program can have several cycles of heating and pulling, each defined by a line of parameters:

- *Heat* specifies the laser output power, and thus the amount of energy absorbed by the tube, during the soft pull.
- *Fil*ament specifies the laser beam scanning pattern used, which determines the power distribution and the rate of the scan.
- *Vel*ocity specifies the target velocity, corresponding to the viscosity and hence to the temperature, at which the hard pull is initiated.
- *Del*ay specifies the time delay between the deactivation of the laser and the hard pull. These two can be timed to occur either simultaneously or one can precede the other.
- *Pull* specifies the force of the hard pull.

For most of the tips presented here we used the following two line program

	heat	fil	vel	del	pull
line 1	750	5	20	135	122
line 2	640	4	74	135	80

After pulling the tips, they are cut and inserted into a grid of eight tips. Gold contacts are then deposited on both sides of the cylindrical part of the tips, where a mask covers their tapered part and restrict the contacts to a narrow strip to prevent overlapping.

The deposition is done in a vacuum chamber, using e-beam evaporation, a thin layer (8 nm) of chromium is deposited to enhance the adhesion of the gold contacts, 200 nm thick, then deposited. This procedure is repeated on the opposite side of the grid.

The tips are then rotated by 90°, to verify this the side contacts should not be visible. The tips are then had to be carefully aligned so that the shunt, a narrow strip of chromium and gold, is deposited on the tip through a suitable mask which covers the entire grid except a slit of about 300 μm width.

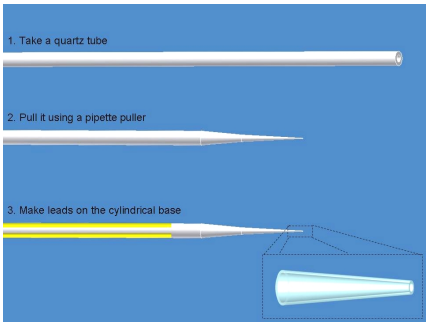

Figure 12: A schematic drawing of the first two stages. The tapered region is covered as shown in the bottom-right corner.

After the SQUID is deposited, as explained in section 3.2, the shunt shunts the superconducting electrodes in parallel with the junction. The position of the shunt on the tip determines its resistivity, since the closer it is to the apex the shorter the bridge is. Also the distance from the tip affects the parasitic inductance between the shunt and the junction.

The first shunts were composed of 8 nm chromium and 10 nm of gold, and further shunts were modified from this starting point, see Fig. 13.

The procedure of the shunt alignment is not very accurate and a lot of time is wasted in pushing the tips back and forth under the microscope trying to locate a tip on the optimal position. Recently a novel design for a grid had been fabricated, in which the mask itself can be manipulated to relocate each slit seperately. Moreover, the slits in this grid are 200 μm wide, so modifications in thickness result in smaller resistance variation which gives us greater control.

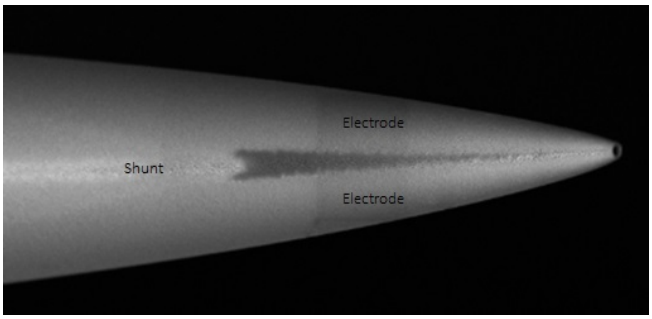

Figure 13: SEM image of a ShOT (Shunt On Tip), located 20 μm away from the tip apex.

A single tip is then inserted into a tip holder which has a groove, which is used as bottom contact, and a spring as a top contact. The tip is then placed and fixed,

and electrically connected to suitable contacts on the tip holder. This method requires no wire-soldering on the tip itself, and is fast and easy to manipulate. A shorting screw is implemented on the top contact which can be screwed down to the bottom to avoid electrical breakdowns that can damage the tip.

This method, however, has a major drawback since the top contact has very high parasitic resistance, up to 10 Ω, resuting in very moderate loadline. We isolated the contact resistance and discovered that a thin layer of indium, a soft metal, on top of the gold contacts can significantly lower the contact resistance, and we achieved resistances as low as 30 mΩ. The gold contacts are still required though, because the thick indium cannot be applied all the way to the tapered part of the tip, since it might shadow further depositions.

3.2 SOT Deposition

The next step is to deposit the body of the SOT, the Pb contacts and loop. Due to the high surface mobility of Pb, the deposition has to be done at low temperature. The tip holder is mounted on a cryostat, thermally coupled to liquid helium, but since quartz is not a good heat conductor, after the cryostat had been cooled down to $\sim 8K$, low pressure cold helium gas is introduced into the chamber for additional 15 minutes, and pumped out before deposition.

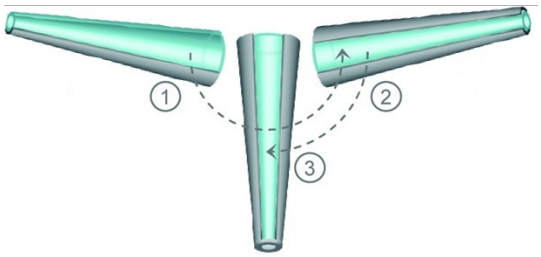

Figure 14: The SOT deposition procedure.

The three stage deposition is done *in situ* using a rotator, as shown scematically in Fig. 14. The first contact is deposited after the tip is inclined by $100 - 115°$, the second contact is deposited on the other side, and the final deposition is the loop at 0°. The contacts are about 25 nm thick, and the ring thickness is $15 - 17$ nm.

The exact inclination depends on the pulling program used, and thus on the tip geometry. While too small inclination will make 'islands' of lead shorting the two contacts, and too large inclination will make the weak link too weak, and I_c will be too low.

3.3 SOT Operating Circuit

The SOT is now ready to operate. The tip holder is mounted into the circuit described above in section 1.6 with some additional filtering, as shown in Fig. 15. We have several such probes, each with a bit different circuit, and mainly used the characterization probe and the microscope probe, which have R_s of 0.58 Ω and 1 Ω respectively. The exact values of the resistors are obtained from measuring the Johnson noise with a shorted circuit.

The probe is wired with four outer terminals, two are the V_{bias} terminals, and two are for the current measurment. The SSAA terminal is connected to a preamp box through which it is biased and its voltage is measured. The voltage readout from the preamp is connected through a feedback box to the fourth terminal which is connected, through a feedback resistor R_{fb}, to a coil coupled to the SSAA. The feedback box drives current through the coil to compensate for the current through the SOT such that the voltage on it will be zero. The voltage on the feedback resistor is then proportional to the SOT current.

The circuit is biased using a YOKOGAWA 7651 source, and the FB voltage is read using an HP 34401A DMM.

The circuit is implemented on a probe which is inserted into a liquid helium dewar. The probe is sealed and pumped, some helium exchange gas is introduced, and it is then lowered into the dewar gradually.

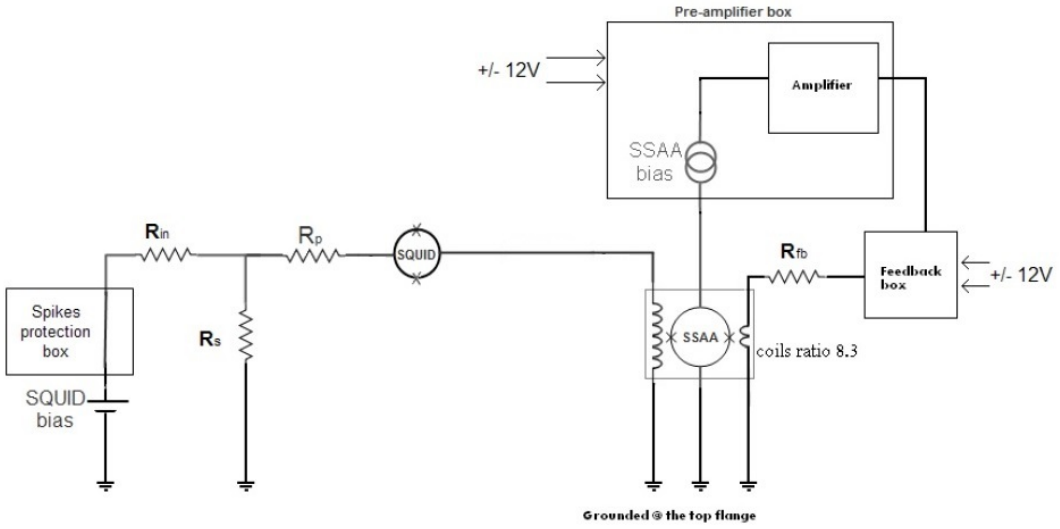

Figure 15: Simplified scheme of the electrical circuit.

3.4 Data Processing

The characterization protocol consists of sweeping V_{bias} up and down, every such sweep is written as a vector. When the bias range of interest is found, we sweep over magnetic fields, using a superconducting magnet inside the dewar, and storing each I-V as a row in the matrix.

The raw data can be seen in Fig. 16a. The voltage on the feedback resistor, V_{fb}, is plotted vs. V_{bias}. Each curve corresponds to a different magnetic field H.

To visualize the SOT response, it is useful to plot the entire I-V-H map. In Fig. 16b V_{fb} is plotted vs. V_{bias} and H, and in Fig. 16c we plot $\frac{\partial V_{fb}}{\partial H}$, which is the actual magnetic response at each point in the $V - H$ plane.

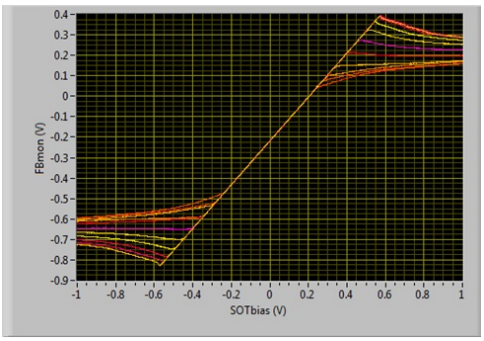

(a) Raw data of V_{fb} vs. V_b for different fields.

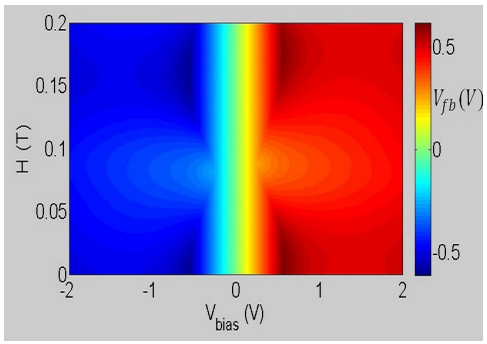

(b) A 2D plot of V_{fb} vs. V_b and H.

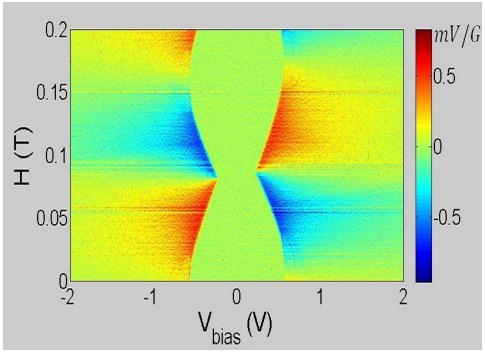

(c) Derivative of (16b) w.r.t. the field. The response is seen to be maximal around I_c at fluxes around $\Phi_0/4$.

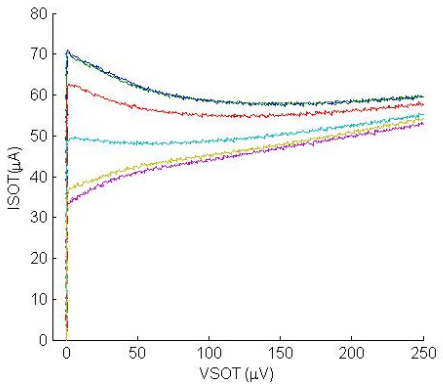

(d) The SOT I-V curves for different fields (selected), extracted from (16a)

Figure 16: I-V-H characterization of the SOT.

For better understanding of the SOT itself it is necessary to extract the true SOT I-V from the data. Using a simple MATLAB code we extract R_p from the

zero voltage regime, and then we can isolate the SOT I-V. This is plotted in Fig. 16d.

3.5 SOT Parameters Extraction

The next step is to extract I_c from each curve, this is rather straightforward. A graph of I_c vs. H is plotted in Fig. 17.

Using equations (14)-(16) and setting $V = 0$, i.e. $\dot{\delta}_{1,2} = 0$, we can find, for a given set of SOT parameters, I_0, L, and asymmetry parameters for both, the maximal supercurrent at a given flux $I_c(H)$, this is done using a MATLAB code written by Dorri Halbertal. The SOT parameters thus can be obtained by fitting the curve to the one was measured.

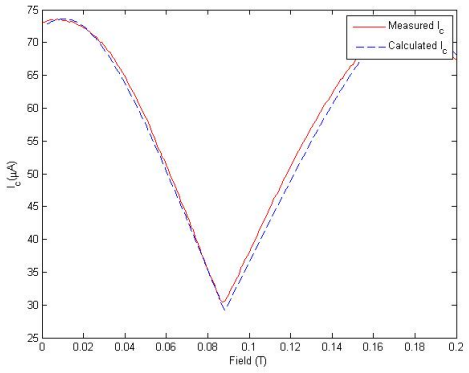

Figure 17: I_c vs. H figure. A good agreement between measurment and reconstructed I_c is seen.

The SOT normal resistance can be extracted from the I-Vs at high currents where the major part of the current is ohmic. However, for underdamped SOTs this requires relatively high current to pass through the SOT branch, and with low shunt resistor, the SOT resistivity at such currents requires very high bias current.

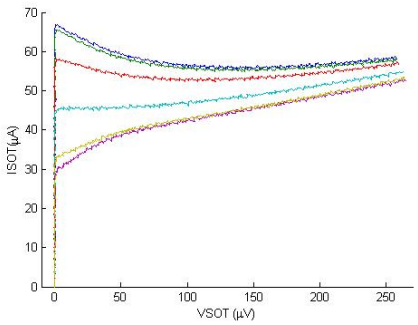

(a) 4.8K I-V. Normal state resistance cannot be deduced.

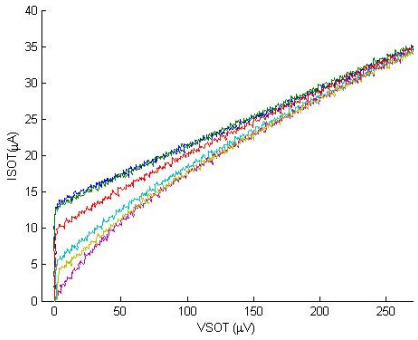

(b) 7.7K I-V. Ohmic behavior is observable at higher bias.

Figure 18: I-Vs at different temperatures. The actual temp. of the SOT is lower than 4.8K and 7.7K measured by a thermometer away from the tip.

Recently, when started the temperature dependence measurments, we discovered that at high enough temperature the critical current is very low and the SOT is usually overdamped which makes normal resistance measurement much easier, as demostrated in Fig. 18.

3.6 β_c Evaluation

As explained in section 1.5, for $\beta_c \geq 1$ the SQUID shows hysteretic behavior, and the value of β_c can be estimated according to equation 13. However, this is true only in current bias while the loadline clearly affects the actual return current.

The current–bias–return–current can be generalized to be bias independent though, recall that the physical meaning of I_r is that it is the lowest current for which there exists a nonzero voltage configuration. Hence we can apply this to any underdamped SQUID to characterize it by this measure i_r, as shown in Fig. 19.

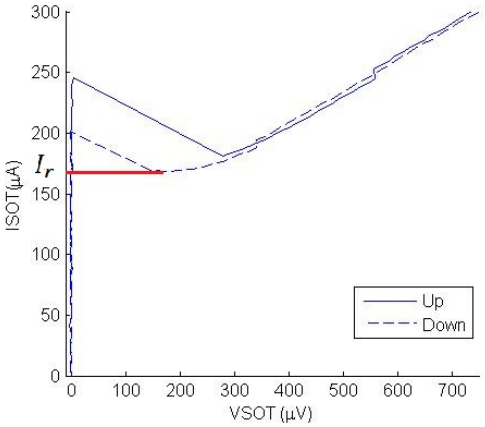

Figure 19: Loadline hysteresis. The generalized I_r is extracted from the 'sweep down' I-V.

4 Results

4.1 First Attempts

In the first stage several SOTs were made with a 10 nm thick shunt about 1 mm away from the tip apex. Despite the resistive shunt these SOTs have shown clear underdamped behavior and hysteresis. Two such I-Vs are shown in Fig. 20. It can be seen that the degree of hysteresis reduces as the magnetic field increases. We will discuss this later in section 4.5.

Their normal resistances were estimated around 3 Ω, much smaller then tens of ohms estimated for intrinsic SOT resistance, so high damping was expected. It was suspected that the shunt was too far from the tip so the impedance due to parasitic inductance was too high in order to eliminate the hysteresis. We therefore decided to try depositing the shunts on the very end of the tips, which we gave the acronym 'ShOVET'.

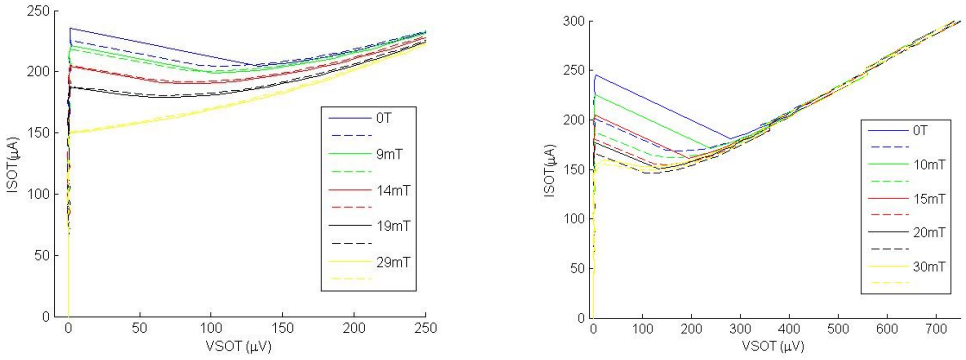

Figure 20: I-Vs of two different SOTs at various magnetic fields.

4.2 Closer Shunts (The 'ShOVET' Era)

To make a ShOVET the tips have to be manipulated carefully in the grid, while looking at them in optical microscope. It is impossible to accurately locate the tip at the edge of the shunt slit, so in order to keep the parasitic inductance as low as possible we tried to align the

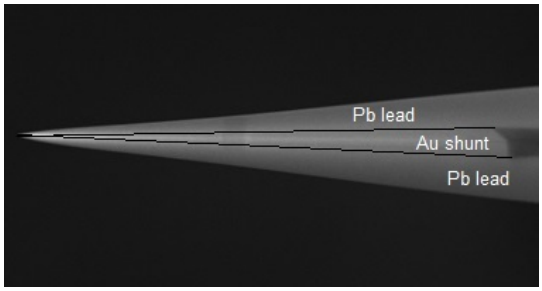

Figure 21: SEM image of a ShOVET

tips such that they are a bit below the
end of the slit.

Moving the shunt to the end also was thought to significantly decrease the resistance, because at the end of the tip the shunt is mach shorter, but it was not found to be the case. Several explanations have been suggested:
Firstly, a quick derivation shows that the trimmed triangular resistor should have lower resistance by only a factor of order 4 than the approximately rectangular far shunt. Adding to that the fact that the ShOVET is sometimes half the width of a far shunt, as explained above, may explain the small variance.
Secondly, with such a thin layer of gold, surface oxidization highly affects the resistance of the shunt, added to the above-mentioned considerations, this makes the resistance much less controllable.

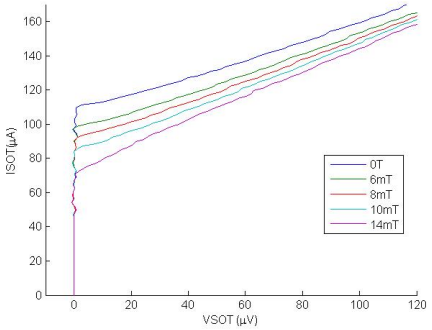

(a) SOT #130411, $R_N \approx 1.4\ \Omega$.

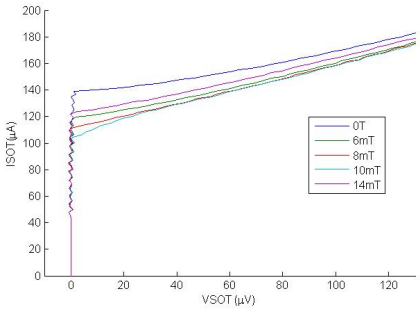

(b) SOT #130415, $R_N \approx 1.7\ \Omega$.

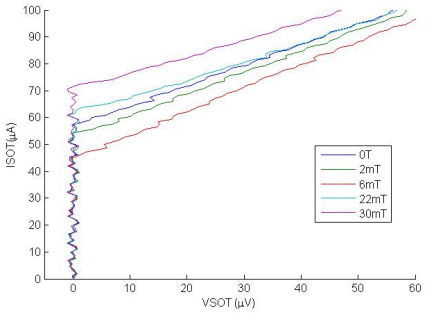

(c) SOT #130428, $R_N \approx 1.2\ \Omega$.

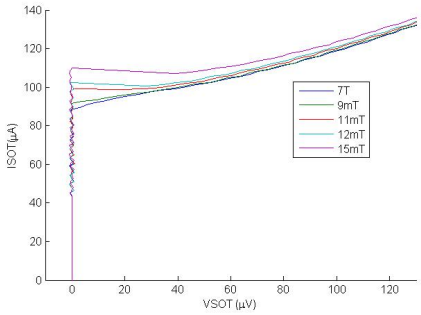

(d) SOT #130430, $R_N \approx 2.5\ \Omega$. A slightly negative slope is visible.

Figure 22: ShOVETs.

We attained several highly overdamped SOTs with SHOVETs that showed promising characteristics as shown in Fig. 22. We have noticed however that crit-

ical current was lower than usual, and a few tips showed neither field dependence nor even critical current. We suspected that the ShOVET suppresses superconductivity in the weak links through proximity effect. So we decided to try to deposit the shunts a few microns away from the tip apex.

4.3 Moving the Shunt Away from the Tip Apex

Depositing the shunt 'close' to the tip is even harder than making a ShOVET, where you can align the end of the tip within a 200 μm wide slit in the mask whereas for 'ShNOVETs (Shunt *Not* On the Very End of the Tip') a more precise alignment of the distance from the tip apex is required.

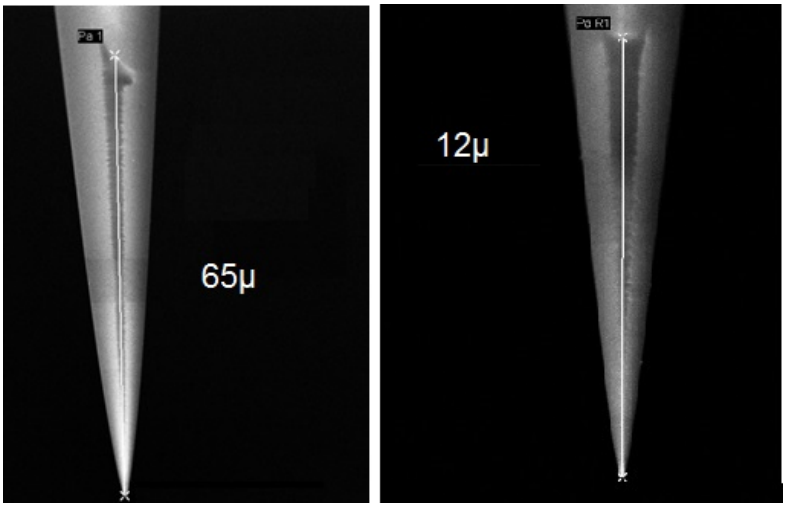

Figure 23: SEM image of two ShNOVETs

It seems that this approach has solved the proximity problem, since no more 'no junction' SOTs were measured and the yield improved. We then focused on making the 'marginally damped' SOT, instead of highly overdamped ones, by making the shunt thinner and thinner. But because the shunts were initially very thin, we had to play with small variations which did not always give expected results.

Correlation between the resistance and the damping is not clear, while the SOT in Fig. 24d exhibits marginally-damped behavior with high normal resistance, the SOTs in Fig. 24a is clearly underdamped and the SOTs in Fig. 24b-c show very different behavior at similar resistance.

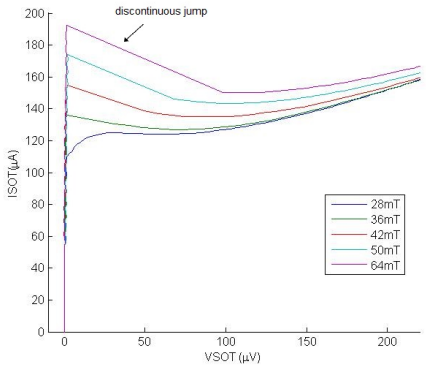

(a) SOT #130522, $R_N \approx 2.5\ \Omega$.

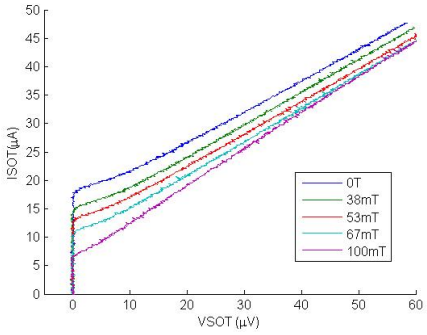

(b) SOT #130617, $R_N \approx 1.4\ \Omega$.

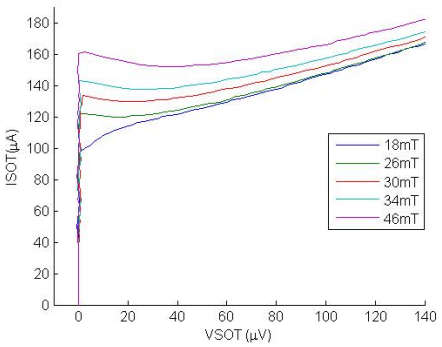

(c) SOT #130625, $R_N \approx 1.6\ \Omega$.

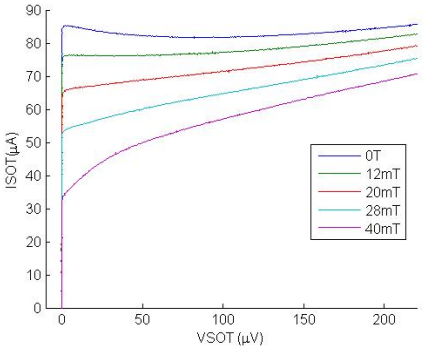

(d) SOT #130818_2, $R_N \approx 7\ \Omega$.

Figure 24: ShNOVETs. The shunts of SOTs a-c were made with thicknesses of 10 nm, 8 nm and 6.4 nm respectively, while SOT d, was made with 5 nm shunt, where we observe a large change in the resistance.

4.4 Parasitic Resistance Reduction

At this point we explored how to reduce parasitic resistance that was typically in the range between few ohms and 20 ohms. It was suspected that the major contribution comes from the top contact between the spring and the gold strip on the tip. It was suggested that indium, due to its softness, is more suitable for this kind of contact.

We measured the resistance of a tip shorted with a big chunk of indium, using four wire measurment, and it turned out that indium contacts can reduce the parasitic resistance from the several ohms we were used to, to few tens of milliohms.

This was a great progress, since a low parasitic resistance allows even underdamped SOTs (with negative differential resistance) to be measured without jumps and hysteresis, due to the much steeper loadline. Fig. 25 shows I-Vs of two un-

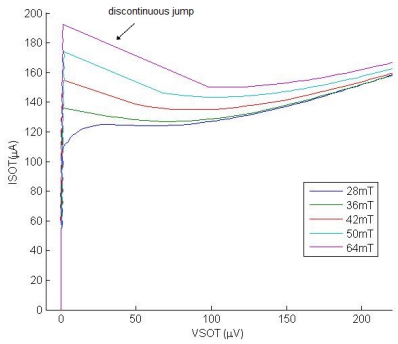

(a) SOT #130522 with gold contacts, $R_p = 1.4\ \Omega$.

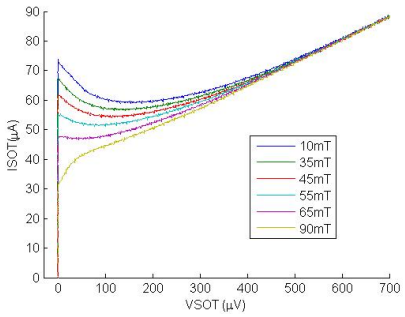

(b) SOT #130908 with In contacts, $R_p = 0.3\ \Omega$.

Figure 25: Underdamped SOTs with different loadlines.

derdamped SOTs: (a) with gold contacts and (b) with indium contacts. It can be seen that while the former is jumpy, the latter has smooth continuous curve. Generally, shunting is still necessary to keep the SOTs in the non-jumpy regime.

4.5 Flux Modulated Damping

At this point we have accumulated enough data to try to understant the results described above. Most of the underdamped SOTs showed overdamped behavior at some applied fields (see Fig. 20(a)), even SOTs with relatively high underdamped behavior. We therefore assumed that this behavior is due to the different dynamics of the SQUID in the presence of flux, and not only through reducing the critical current and thus β_c.

At this point I suggested the 'generalized return current' as a quantity to characterize an underdamped SOT, as explained in section 3.6. We therefore plotted $\beta_c = [2-(\pi-2)i_r]/i_r^2$, as obtained from the return current I_r, for different curves of a given SOT.

The finding were the following:

- Most underdamped SOTs have β_c of order unity.
- The dependence of β_c on I_c is linear as expected if the flux dependence is only due to change of I_c.
- The slope is much steeper than expected if the assumptions which led us to equation 17 was valid, so apparently the flux plays a major role here.

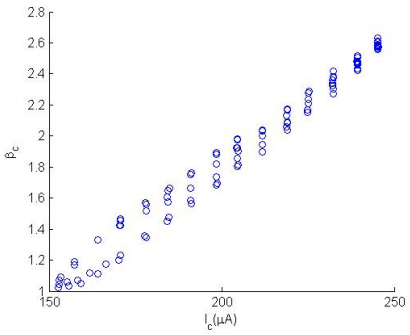

(a) SOT #130408, shown in Fig. 20(b) damping vs. I_c.

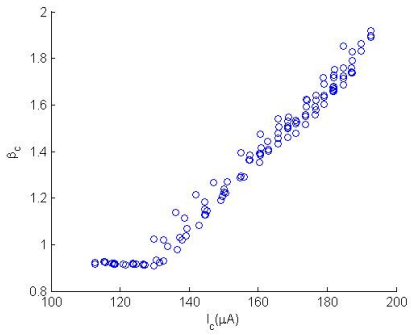

(b) SOT #130522, shown in Fig. 24(a) damping vs. I_c.

Figure 26: β_c vs. I_c plotted for two different SOTs. Linear behavior is observable, but reduction to about 70% in I_c resulted in lowering β_c in half.

At fluxes close to $n\Phi_0$ the circulating current is small, thus we assumed that inductance effects are negligible and equation (17) is still valid, and β_c obtained at the maximal value of I_c is still believed to well characterize the SOT.

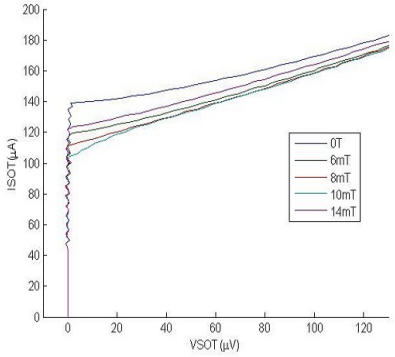

(a) SOT #130415, liquid helium $T = 4.2K$.

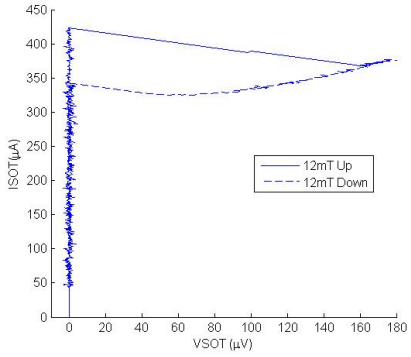

(b) SOT #130415, ^3He system, $T = 250$ mK.

Figure 27: SOT characteristic at different temperatures.

One of the SOTs was measured both in our liquid helium system and in the ^3He system (250 mK), the results are shown in Fig. 27. It can be seen that while at 4.2K an overdamped behavior is observed, at 250 mK the response is jumpy and hysteretic. Fig. 27b corresponds to $\beta_c \approx 1.75$, so if RCSJ is valid at zero flux, we can predict that overdamped behavior will show up when I_c will be low enough such that $\beta_c = 1$, this will occur around $I_c = \frac{420}{1.75} = 240$ μA, in agreement with Fig. 27a. This measurement led us to further understand that temperature

dependence measurments are the key in comparison with RCSJ.

4.6 Temperature Dependence Measurement

To carry out temperature dependence measurments we use a heater and the thermometer that are located about 5 mm below the tip.

We fully characterized few SOTs at different temperatures, from the base $4.2K$ to around $8K$.

4.6.1 Temperature Dependence of I_c

The first, and most obvious measurment is the dependence of the critical current. Results for three different SOTs are plotted in Fig. 28, alongside with their linear fit.

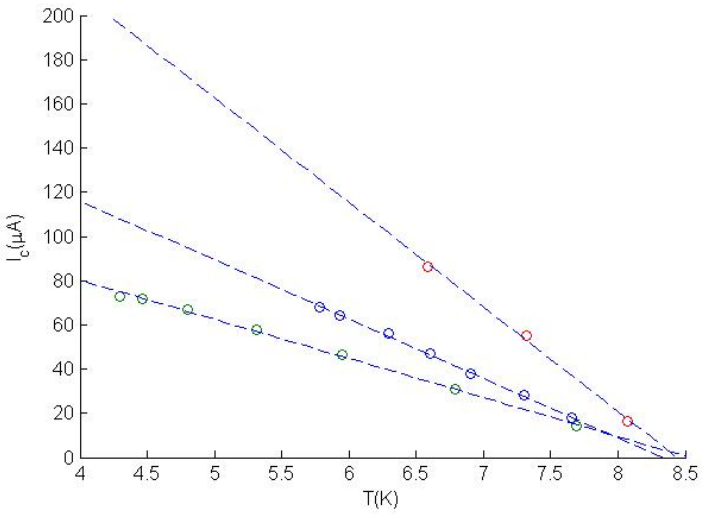

Figure 28: I_c vs. T for three SOTs.

We notice that the three measurments have very good linear fit, and that they cross almost at the same point, which is expected to be $T_c = 7.2K$. The deviation from this is a consequence of temperature difference between the SOT and the thermometer. Further investigation has to be done to utilize the SOT as a 'two in one' magneto-thermo-meter.

4.6.2 Damping at Different Temperatures

The initial motivation of these measurments was to compare the change of damping caused by magnetic flux with that caused by changing the temperature. We plotted again the damping against critical current, but at a variety of temperatures. The results are shown at Fig. 29.

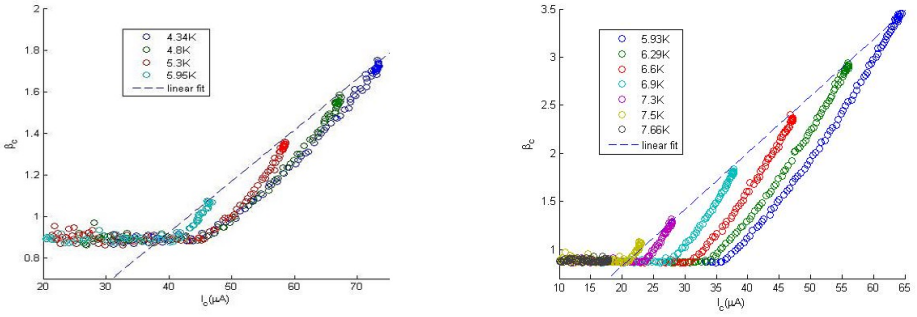

(a) SOT #130908. (b) SOT #130908_2.

Figure 29: β_c vs. I_c at various temperatures plotted for two different SOTs.

The difference between 'flux damping' and 'temperature damping' is remarkable, while the flux-damping, shown in Fig. 29 for each temperature is very steep, and approach $\beta_c = 1$ fast, the temperature-damping at zero flux, represented by the dashed line is much more moderate and is consistent with the RCSJ prediction of $\beta_c \propto I_c$. Moreover, the slopes of the two fits are with ratio $2.39 = 1.54^2 = \left(\frac{R_2}{R_1}\right)^2$, in agreement with RCSJ predictions that $\beta_c \propto R^2$.

4.6.3 Temperature Dependence of the Inductance

The inductance can be extracted from the I_c curves, as explained in section 3.5. I_c curves at different temperatures are shown for two SOTs in Fig. 30.

The curves were reconstructed with very good agreement as shown in Fig. 31, and shows, besides I_c discussed above, temperature independent parameters. SOT #130908, showed temperature independent inductance of 17.6 pH from 4.3 K to 7.3 K, and SOT #1309082 showed constant inductance of 22 pH for a similar range of temperatures, both values much higher than expected from geometrical considerations.

The geometrical contribution to the inductance should not be affected by the temperature change. On the other hand, the kinetic inductance is due to the inertial motion of the superconducting electrons. As the temperature increases, the

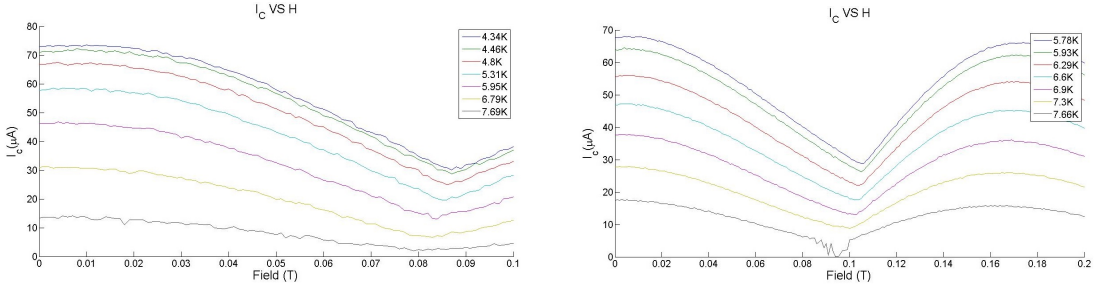

(a) SOT #130908.

(b) SOT #1309082.

Figure 30: I_c vs. H curves at various temperatures plotted for two different SOTs.

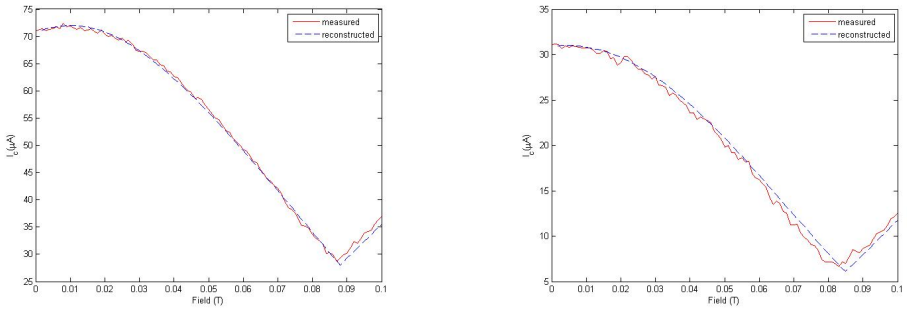

(a) SOT #130908 at $4.46K$. The I_c curve was simulated for $L = 17.6$ pH, identical junctions with $I_{c1} = I_{c2} = 36$ μA and inductance assymetry $\alpha_L = 0.2$.

(b) SOT #130908 at $6.79K$. The parameters are the same as in (a) except $I_{c1} = I_{c2} = 15.5$ μA

Figure 31: Reconstructed I_c curves at different temperatures, the same SOT parameters were used.

superconducting electrons density, n_s, decreases, so higher velocity is required for a certain value of current, which means higher kinetic energy and inductance. The kinetic inductance depends inversely on n_s so it should increase with temperature.

4.7 SOT Capacitance Estimation

Although linearity of β_c in I_c has been observed, confirmation of the R^2 dependence requires comparison between different SOTs, for which the capacitance might differ significantly. Plotting β_c against I_cR^2, assuming the SOTs have the same capacitance gave meaningless results, as the distribution is far from a straight line, and bares no information.

We can, however, try to estimate the value of the capacitance, based upon RCSJ and the data acquired. We have thirteen underdamped SOTs contributing to this, as overdamped SOTs give us no information since β_c cannot be evaluated. The capacitances range from 60 fF(three SOTs) through hundreds of femto-farads (average 400 fF) up to 1 pF. These all are reasonable values according to past estimations.

5 Discussion and Conclusions

5.1 Agreement with RCSJ

We generalized the return-current parameter and confirmed the linear dependence of β_c on I_c. However we could not find a consistent evidence for the R^2 dependence.

The flux controlled damping has been found to deviate significantly from the simplified Eq. 17, as overdamped behavior shows up at critical currents at which β_c is still larger than one. For measurements at high fields a SOT with relatively light damping can be used, but addition study is requied before special design for high field SOTs will be possible.

5.2 External Shunting Works

We can certainly say that external shunting works, even hundreds of microns away from the SOT loop, as we managed to make damped SOTs with high critical current, which was not possible previously. However, as the R dependence and capacitance values are not yet known, desiging SOTs with desirable parameters is still done in small steps of trial and error.

5.3 Do We Need Overdamped SOTs?

At this stage it seems that the optimal configuration in terms of noise is to use slightly underdamped SOTs with steep loadline, for optimal response, and the SOT resistance can be higher to reduce noise. More carefull optimization is of course still required. On the other hand slightly overdmped SOTs using shunt on tip are highly advantegeous, especially for devices with high currents, to prevent jumpiness over the entire range of magnetic fields.

5.4 Temperature Dependence

We have found that I_c is very close to linear in temperature in the region of $T > 4.2$ K, and it might be used to measure a sample temperature while scanning. The behavior of Pb SOTs at lower temperatures has to be studied.

We have found surprisingly that inductance seems to be temperature independent, this in apparent contradiction with our assumption that most of it originates from the kinetic part. This might also be subject for furter investigations.

References

[1] Likharev, K. K. Superconducting weak links. *Rev. Mod. Phys. 51(1), 101159*, Jan (1979).

[2] M. Tinkham, Introduction to superconductivity, *McGraw-Hill*, 1995.

[3] V. Ambegaokar and A. Baratoff, *Phys. Rev. Lett. 10, 486 (1963); erratum, I1, 104*, 1963.

[4] I.O. Kulik and A.N. Omel'yanchuk, *Zh. Eskp. Teor. Fiz. Pis. Red. 21,216*, 1975; *Lett. 21, 96*, 1975; *Fiz. Nizk. Temp. 3, 945*, 1977; *Sov. J. Low Temp. Phys. 3, 459*, 1978.

[5] F. London, Superfluids, *Wiley, New York*, 1950.

[6] R.C. Jaklevic, J. Lambe, A.H. Silver, and J.E. Mercereau, *Quantum interference effects in Josephson tunneling, Phys. Rev. Lett. 12, 159160*, 1964.

[7] J. Clarke and A.I. Braginski, *The SQUID Handbook: Fundamentals and Technology of SQUIDs and SQUID Systems, Volume I. Wiley-VCH, Berlin, first edition*, 2004.

[8] D. Vasyukov, Y. Anahory, L. Embon, D. Halbertal, J. Cuppens, L. Neeman, A. Finkler, Y. Segev, Y. Myasoedov, M.L. Rappaport, M.E. Huber, and E. Zeldov, *A scanning superconducting quantum interference device with single electron spin sensitivity, Nature Nanotech. 8, 639*, 2013.

[9] R. Meservey, P.M. Tedrow,*Measurements of the kinetic inductance of superconducting linear structures, J. Appl. Phys. 40, 20282034*, 1969.

[10] N.C. Koshnick et al, *A terraced scanning superconducting quantum interference device susceptometer with submicron pickup loops. Appl. Phys. Lett. 93, 243101*, 2008.

[11] A. Finkler, Y. Segev, Y. Myasoedov, M. L. Rappaport, L. Neeman, D. Vasyukov, E. Zeldov, M. E. Huber, J. Martin and A. Yacoby, *Self-aligned nanoSQUID on a tip, Nano Letters 10, 1046*, 2010.

[12] A. Finkler, D. Vasyukov, Y. Segev, L. Neeman, Y. Anahory, Y. Myasoedov, M.L. Rappaport, M.E. Huber, J. Martin, A. Yacoby and E. Zeldov,*Nano-sized*

SQUID-on-tip for scanning probe microscopy,J. Phys.: Conf. Ser. 400, 052004, 2012.

[13] A. Finkler,*Scanning SQUID Microscope for Studying Vortex Matter in Type-II Superconductors, Springer Theses, Springer*, 2012.

[14] A. Finkler, D. Vasyukov, Y. Segev, L. Ne'eman, E.O. Lachman, M.L. Rappaport, Y. Myasoedov, E. Zeldov, and M.E. Huber,*Scanning superconducting quantum interference device on a tip for magnetic imaging of nanoscale phenomena, Rev. Sci. Instrum. 83, 073702*, 2012.

[15] W.C. Stewart, *Current-Voltage characteristics of Josephson junctions, Appl. Phys. Lett. 12, 277280*, 1968.

[16] H. Zappe, *Minimum current and related topics in Josephson tunnel junction devices, J. Appl. Phys. 44, 13711377*, 1973.

[17] C.D. Tesche and J. Clarke, *dc SQUID: noise and optimization, J. Low Temp. Phys. 29, 301331*, 1977.

[18] K.K. Likharev,*Dynamics of Josephson Junctions and Circuits. New York: Gordon and Breach*, 1986.

[19] R.P. Welty, J.M. Martinis, *A series array of dc SQUIDs, IEEE Trans. Magn. 27, 29242926*, 1991.

[20] M.E. Huber, P.A. Neil, R.G. Benson, R.G., D.A. Burns, A.M. Corey, C.S. Flynn, Y. Kitaygorodskaya, O. Massihzadeh, J.M. Martinis, G.C. Hilton, *DC SQUID series array amplifiers with 120 MHz bandwidth, IEEE Trans. Appl. Supercond. 11, 12511256*, 2001.

[21] P.K. Hansma, G.I. Rochlin and J.N. Sweet, *Externally Shunted Josephson Junctions: Generalized Weak Links, Physical Review B, vol. 4, Issue 9, pp. 3003-3014*, 1971.

[22] T.A. Fulton, *Externally Shunted Josephson Junctions, Physical Review B, vol. 7, Issue 3, pp. 1189-1193*, 1973.